Geochemical Characterization of Coal-Combustion Byproducts and Numerical Simulations of their Long-term Effects as Capping Materials at Coal Mine Reclamation Sites

Zhang, Qian[1,2]; Olyphant, Greg[1]; Branam, Tracy[2]; Ghanem, Hind[1].

[1] Department of Geological Sciences, Indiana University, Bloomington, IN 47405
[2] Indiana Geological Survey, 611 North Walnut Grove Ave., Bloomington, IN 47405

CONFERENCE: 2015 World of Coal Ash – (www.worldofcoalash.org)

KEY WORDS: coal-combustion byproducts, reclamation, reactive transport modeling, sequential extraction, trace elements

1. Introduction

Coal combustion byproducts (CCBs) generated from coal-fired power plants, such as fly ash, bottom ash, and flue gas desulfurization (FGD) materials, have increased during the past decades, because coal is the one of the world's primary energy source. In 2009, more than 125 million tons of coal-combustion byproducts were generated in the United States, while only 44% were used beneficially.[1] Intensive studies on the chemical composition of CCBs from various coal-fired power plants that provide detailed mineralogical and geochemical compositions of CCBs have been conducted.[1-10] Among CCBs, fly ash is the most studied byproduct; it displays variable multicomponent and heterogeneous compositions, depending on the source of coals and operating conditions at power plants.[10, 11]

One beneficial use of CCBs is as structural fill and capping material in abandoned mine land (AML) reclamation sites because of their low cost, availability, and capacity for neutralizing acid.[12] By mixing flue gas desulfurization sludge, fly ash, and lime, a low-permeable, cementitious substance—fixated scrubber sludge (FSS)—is generated.[13, 14] Previous studies focused on the geochemical characterization of FSS derived from mineral composition data obtained by X-ray diffractometric analysis.[15] Results show that FSS is a complex mixture of amorphous phases and crystalline minerals, as well as other minor and trace elements. Recent leaching experiments also confirmed the existence of certain trace elements by observing enhanced concentrations of boron, chromium, molybdenum, barium, and nickel in the leachate.[16] However, few studies have comprehensively examined the impacts of CCBs that were emplaced in actual field settings. For modeling purposes, it is important to closely examine the chemical

phases that contain trace elements and to characterize the morphology of CCBs that are subjected to ambient weathering processes.

This research continues the work of previous studies on FSS.[15,16] Our purpose is to examine the microstructure of FSS, quantify the elemental composition of the most abundant phase (amorphous phase), and identify the solid phases that contain trace elements, thereby gaining a more comprehensive mineralogical and geochemical understanding. A combination of scanning electron microscopy (SEM), electron microprobe (EMP) analysis, and sequential extraction procedure was used to achieve these goals. Understanding the mineral phases, chemical composition, morphology, and distribution of trace elements in FSS is critical in assessing the risk of the potential environmental mobility of toxic trace metals. The availability and mobility of trace metals in CCBs depend on the physical and chemical properties of FSS. Moreover, the data obtained from these analyses are necessary for numerical modeling.

In this study, numerical simulations of coupled reactive and transport processes were used to address the long-term issues of how using engineered CCBs affect groundwater quality at an AML site. Emphasis was placed on developing a model for reactive fluid flow and geochemical transport process in an acid mine drainage setting where engineered CCB materials are used as capping materials. The results from this study will facilitate the reuse of solid waste created during coal combustion in an effort to minimize the negative impacts of coal-fired power plants. This may aid in making coal power more sustainable.

2. Material and methods for analytical work

2.1 Study site

In 1996, the Midwestern AML site, located in Pike County, Indiana, underwent reclamation by the Indiana Department of Natural Resources-Division of Reclamation [17] (Fig. 1). At this site, a deposit of coarse-grained pyritic coal refuse was buried under a layer of fixated scrubber sludge composed of FGD material, fly ash, and lime. The FSS was, in turn, overlain by a 1-m-thick soil layer consisting of reworked spoil and animal waste fertilizer, which facilitates revegetation. For 18 years following reclamation, water monitoring was conducted and sediment core samples collected and analyzed. Core samples of the FSS cap were collected at several monitoring well sites in 2011 using a Geoprobe by Martin et al. (2012).[15]

2.2 Sample preparation for morphology and chemical composition analysis

Samples of FSS cores from the Midwestern site were taken from the top (M7-02-t, M8-02-t), middle (M7-02-b, M7-03-m, M8-02-b, M8-03-m) and bottom (M7-03-b, M8-03-b) of FSS layer to identify any changes in morphology associated with weathering and to compare any differences within the FSS. Eight samples were impregnated with Petropoxy, and hardened with stage heating. Using standard polishing techniques, they were then polished to study their internal structure and composition of individual

particles. Each sample was characterized by selecting different fields of view under scanning electron microscopy (SEM), with special focus on the elemental composition and morphology of the amorphous phase. Three samples (M7-02-t, M7-03-m, and M8-03-m) were chosen for electron microprobe analysis; they were re-shaped, slightly repolished, and coated with carbon. The chemical compositions of each type of particle identified under SEM were analyzed using EMP, with two to three spots per grain from each sample.

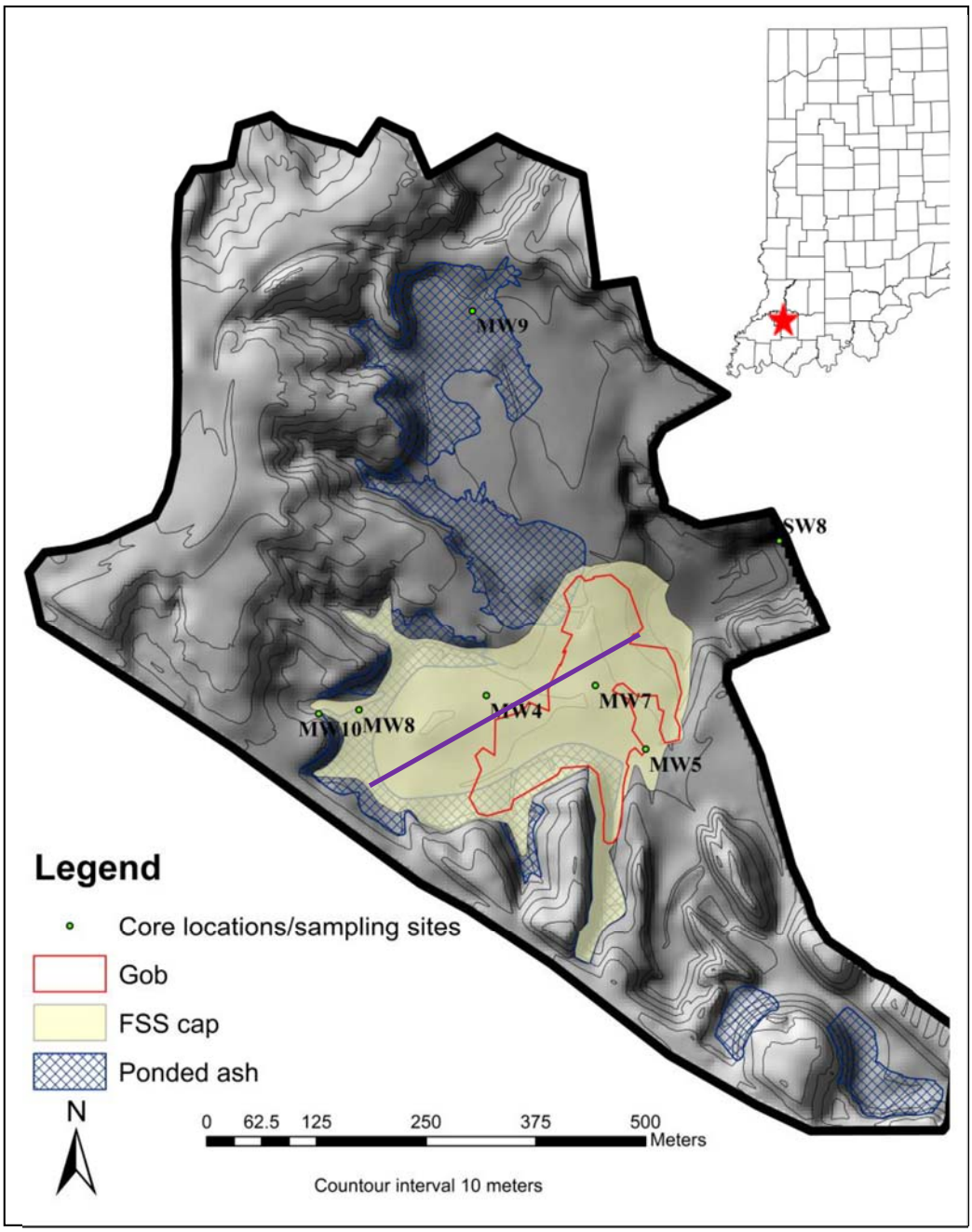

Fig. 1. Location of the Midwestern abandoned mine land site, showing monitoring wells, areas covered by fixated scrubber sludge, coal ash, and gob piles. The solid purple line indicates the cross-section of the numerical model. (After Martin et al., 2013).[16]

2.3 Scanning electron microscopy

The morphological and elemental analyses of the FSS samples were conducted using a FEI Quanta 400 FEG field emission environmental SEM in the Indiana University Shale Research Laboratory. The most common technique for physical and chemical characterization of mineral phases in fly ash,[11, 18] SEM generates images of the sample by scanning the surface with a focused electron beam. Backscattered electron imaging and secondary electron imaging were used to record the images. Energy-dispersive X-ray spectroscopy was used to characterize the morphology and determine the chemical phases.

2.4 Electron microprobe

Quantitative analyses for the amorphous phase were conducted using a CAM-ECA SX 50 electron microprobe with detailed backscattered electron imagery at Indiana University. An accelerating voltage of 15 kV was used with a beam current of 6 nA. The compositions of the amorphous phase were determined by wavelength dispersive analysis.

2.5 Sequential extraction

Analytical procedures involving total and sequential chemical extractions were employed to understand the total amount and partitioning of particulate trace elements. The total concentration of trace elements (As, Ba, Cd, Cr, Cu, Pb, Hg, Mo, Ni, and Zn) were analyzed by Brookside Laboratories using inductively coupled plasma atomic emission spectroscopy. Sequential extraction was conducted at the analytical geochemistry lab at Indiana University. The procedures and chemicals were applied following Tessier et al. (1979),[19] with the slight modification of introducing leaching with deionized water as the first step.[20] The samples were divided into six different fractions: water-washable, exchangeable, bound to carbonates, bound to Fe-Mn oxides, bound to organic matter and sulfides, and residual. Samples were ground and homogenized in an agate mortar, then 2-g FSS samples were used to start sequential extractions. The concentrations of As, Cu, and Zn from the first five extractions were analyzed using atomic absorption spectroscopy, and the concentrations in residuals were calculated using the total concentration minus the sum of first five extractions.

3 Reactive Transport Modeling

3.1 Overview

Numerical simulations were performed using the computer program TOUGHREACT, which is capable of modeling up to three-dimensional geologic domains with physical and chemical heterogeneity. The TOUGHREACT source code was developed as an extension of the non-isothermal multi-phase fluids and heat flow code TOUGH2, the general chemical speciation and reaction package based on EQ3/6.[21-23] Previous research has demonstrated with case studies that TOUGHREACT is capable of

simulating water-rock-gas interactions during fully transient, multiphase, non-isothermal flow and transport in hydrogeologically and geochemically heterogeneous rock media.[24, 25]

3.2 Governing equations

Combining chemical reactions and fluid flow transport, the general governing equation employed in TOUGHREACT to describe geochemical processes involving fluid-rock interactions can be written as follows: [23, 26, 27]

$$\frac{\partial}{\partial t}\emptyset C_i = \frac{\partial}{\partial x}\left(\emptyset \mathbf{D}\frac{\partial C_i}{\partial x}\right) - \emptyset \upsilon \frac{\partial C_i}{\partial x} + \emptyset r_i \quad (1)$$

$$\mathbf{D} = D^* + D_h \quad (2)$$

where C_i is the concentration of a specific species in the pore fluid (mol·m^{-3}), $\emptyset$ is the porosity of the porous media, and υ is the average linear fluid velocity of the flow (m·s^{-1}); r_i is the reaction rate of species i in solution (mol·m^{-3}·s^{-1}); positive values of r_i indicate dissolution, and negative values indicate precipitation. **D** represents the combined molecular diffusion (D^*) and mechanical dispersion coefficient (D_h) for the porous media (m^2·s^{-1})[28]; note that the first two terms on the right side of the equation describe the transport process (diffusion and advection, respectively), and the last term describes the effect of geochemical reactions between solid and liquid phases.

Accurate reactive transport modeling requires appropriate quantitative estimates of kinetic parameters. The kinetic rate of each reaction in TOUGHREACT is calculated using the following general equation to describe the surface-controlled mechanism: [26]

$$r = k * A * [1 - (\frac{Q}{K})^{\theta}]^{\vartheta} \quad (3)$$

where r is the kinetic rate of precipitation/dissolution of a specific mineral (mol·m^{-3}· s^{-1}) (recall that r>0 indicates dissolution, and r<0 indicates precipitation); k is the kinetic rate constant (mol·m^{-2}·s^{-1}); A is the reactive surface area of mineral (m^2·m^{-3}); Q is the dimensionless reaction quotient; K is the equilibrium constant for mineral-water reaction in the form of destruction of 1 mole of mineral; θ and ϑ are fitting parameters that can be determined from experiments, but which are usually taken equal to unity. The value of kinetic rate constant k for a given reaction is commonly calculated using the following equation for neutral pH, acid, and base mechanisms: [29]

$$k = k_{nu}^{25} * \exp[\frac{-E_{nu}^a}{R}\left(\frac{1}{T} - \frac{1}{298.15}\right)] + k_H^{25} * \exp\left[\frac{-E_H^a}{R}\left(\frac{1}{T} - \frac{1}{298.15}\right)\right] * a_H^{nH}$$
$$+k_{OH}^{25} * \exp\left[\frac{-E_{OH}^a}{R}\left(\frac{1}{T} - \frac{1}{298.15}\right)\right] * a_{OH}^{nOH} \quad (4)$$

where k^{25} is the rate constant at 25°C (mol·m^{-2}·s^{-1}); R is the ideal gas constant (8.314 KJ·mol^{-1}); T is the absolute temperature (K); E is Arrhenius activation energy (KJ·mol^{-1});

α is the activity of the species (dimensionless); n^H and n^{OH} represent the reaction order with respect to H+, which are commonly set equal to unity if data are not available.

3.3 Preliminary model set-up

To investigate how FSS reacts and at what rate, a uniform FSS layer having a thickness of 1 m and a length of 12 m was used. The reactions between the FSS and groundwater were assumed to be restricted to very thin layers at the top and bottom of the FSS. These thin layers have a saturated hydraulic conductivity of $6.5*10^{-5}$ cm/s, which is 2 orders of magnitude higher than the intact FSS materials (Table 1).[13,14] The higher conductivity is presumed to have developed as a result of imperfect cementation upon placement and subsequent physical and chemical weathering. There are two different environments encountered at the Midwestern site, and two groups of simulations were performed: one focused on interactions between the FSS layer and ambient groundwater at the top thin surface of the FSS layer, and the other focused on interactions between the FSS layer and anoxic mine water along the bottom thin layer of the FSS (Fig. 2). Boundary water was assumed to constantly interact with the FSS layer for 100 years. The geochemical transport simulation also continued for 100 years to investigate the long-term changes in mineral and aqueous compositions of the system. Vertical infiltration was not considered in the preliminary model.

Table 1 Hydrogeologic characteristics of FSS

Physical properties	**FSS[1]**	**Thin layer[2]**
Permeability k (cm^2)	$2.56*10^{-13}$	$1.2*10^{-9}$
Hydraulic conductivity K (cm/s)	$1.4*10^{-8}$	$6.5*10^{-5}$
Porosity φ	0.1	0.2
Density ρ (kg/m^3)	1280	1280

1: From previous investigations
2: Assumed values for the weathered thin layers in the top and bottom of FSS

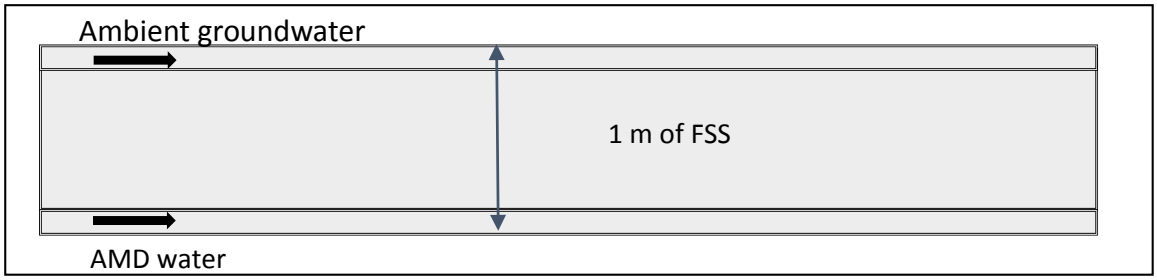

Fig. 2. Schematic diagram of simplified 1-D model for numerical simulations

3.4 Mineral system

The mineralogical percentages of minerals in the FSS layer at the Midwestern site were studied previously,[15] but no detailed information was available about how the trace elements occur within the unreacted FSS materials. Despite this limitation, we used mineralogical data from Martin et al. (1995) [5] in the preliminary simulations as the initial primary mineral composition of the FSS layer (Table 2), while the chemical formula of amorphous phase was obtained from EMP work. Although the current simulations did not evaluate the leaching potential of trace elements, the data provided a reasonable set of initial mineralogical chemistry to undertake the preliminary investigation.

3.5 Geochemical data

Equilibrium constants of most aqueous species and minerals of this study were obtained from the EQ3/6 V7.2b database.[22] There were some additions to the database, including data for ettrringite,[30, 31] hannebachite,[32] mullite,[33] and amorphous glass phases.[34] Most of the mineral reactive surface area data used in this study are based on the work of Sonnenthal et al. (2005),[35] whereas values of amorphous phase, ettringite, hannebachite, and mullite come from other sources.[34, 36-38]

Local equilibrium was assumed to be attained by all reactions among the aqueous species in the model. Kinetic reactions were used for all mineral-water reactions in the model simulations except for more reactive minerals, such as calcite and gypsum, which were considered to be at local equilibrium owing to their fast reaction rates. In most cases, the necessary kinetic parameters are available in Palandri and Kharaka (2004).[29] Kinetic parameters for ettringite, hannebachite, mullite, and amorphous phase were obtained from other published sources.[34, 36-40]

Table 2 Initial mineral volume fractions and possible secondary mineral phases used in the simulations[15]

Mineral assemblage[1]	Chemical formula	Volume percent
Primary		
Amorphous phase[2]	$Si_{0.761}Al_{0.15}Ca_{0.0012}K_{0.004}Mg_{0.0011}Na_{0.0076}O_{1.5301}(OH)_{0.45}$	40
Hannebachite	$CaSO_3.0.5H_2O$	22
Mullite	$Al_6SiO_2O_{13}$	7.6
Hematite	Fe_2O_3	3.5
Quartz	SiO_2	2.5
Gypsum	$CaSO_4.2H_2O$	1.5
Magnetite	Fe_3O_4	1.5
Calcite	$CaCO_3$	1.0
Ettringite	$Ca_6Al_2(SO_4)_3.26H_2O$	0.4
Porosity		20
Secondary		
Kaolinite	$Al_2Si_2O_5(OH)_4$	
Amorphous silica	SiO_2 (am)	
Gibbsite	$Al(OH)_3$	

1: No trace elements were included for the preliminary simulations
2: Chemical formula from EMP work

Average chemistry of the soil water and acid mine drainage at the Midwestern site from previous field and lab studies were used as initial boundary water compositions of the upper and lower FSS layer simulations, respectively (Table 3).

Table 3 Initial chemical concentrations of boundary water

Component	Soil water (mol/L)	AMD (mol/L)
pH	6.1	1.8
$SiO_2(aq)$	$5.36*10^{-4}$	$3.57*10^{-3}$
$O_2(aq)$	$2.54*10^{-4}$	$1.00*10^{-19}$
Na	$1.08*10^{-3}$	$4.35*10^{-4}$
Fe	$8.95*10^{-10}$	$8.06*10^{-3}$
Mg	$3.74*10^{-3}$	$6.17*10^{-3}$
Al	$1.85*10^{-5}$	$1.33*10^{-2}$
K	$1.53*10^{-4}$	$6.91*10^{-4}$
Cl	$2.82*10^{-5}$	$2.82*10^{-5}$
S	$1.00*10^{-2}$	$1.28*10^{-1}$
C	$2.46*10^{-3}$	$1.00*10^{-19}$

4 Results and Discussion

4.1 Particle morphology and chemical composition

The morphology of FSS is controlled by the combustion condition (temperature, pressure) and the subsequent cooling rate. During combustion, the inorganic components in coals were broken down or became volatile and then reacted with oxygen. During the cooling process, they may crystallize as new minerals, amorphous spheroids, or condense as coating on particles.[10] The morphological and elemental analyses from SEM indicated that the FSS samples were composed predominantly of amorphous alumino-silicate spheroids from combustion and hannebachite, the latter mostly derived from oxygen-inhibited flue gas desulfurization sludge. Variability in the morphology of particles observed in the individual samples was common, and the only exception was in sample M7-02-t, which represents the boundary between FSS and the overlying soil layer. In this sample, very few hannebachite crystals were observed; instead, gypsum was present across the whole sample owing to the oxidation of hannebachite in the presence of water and oxygen. The size, shape, and texture of the particles observed display a wide range of heterogeneity. The sizes of the particles varied in the range of <1 to >100 μm.

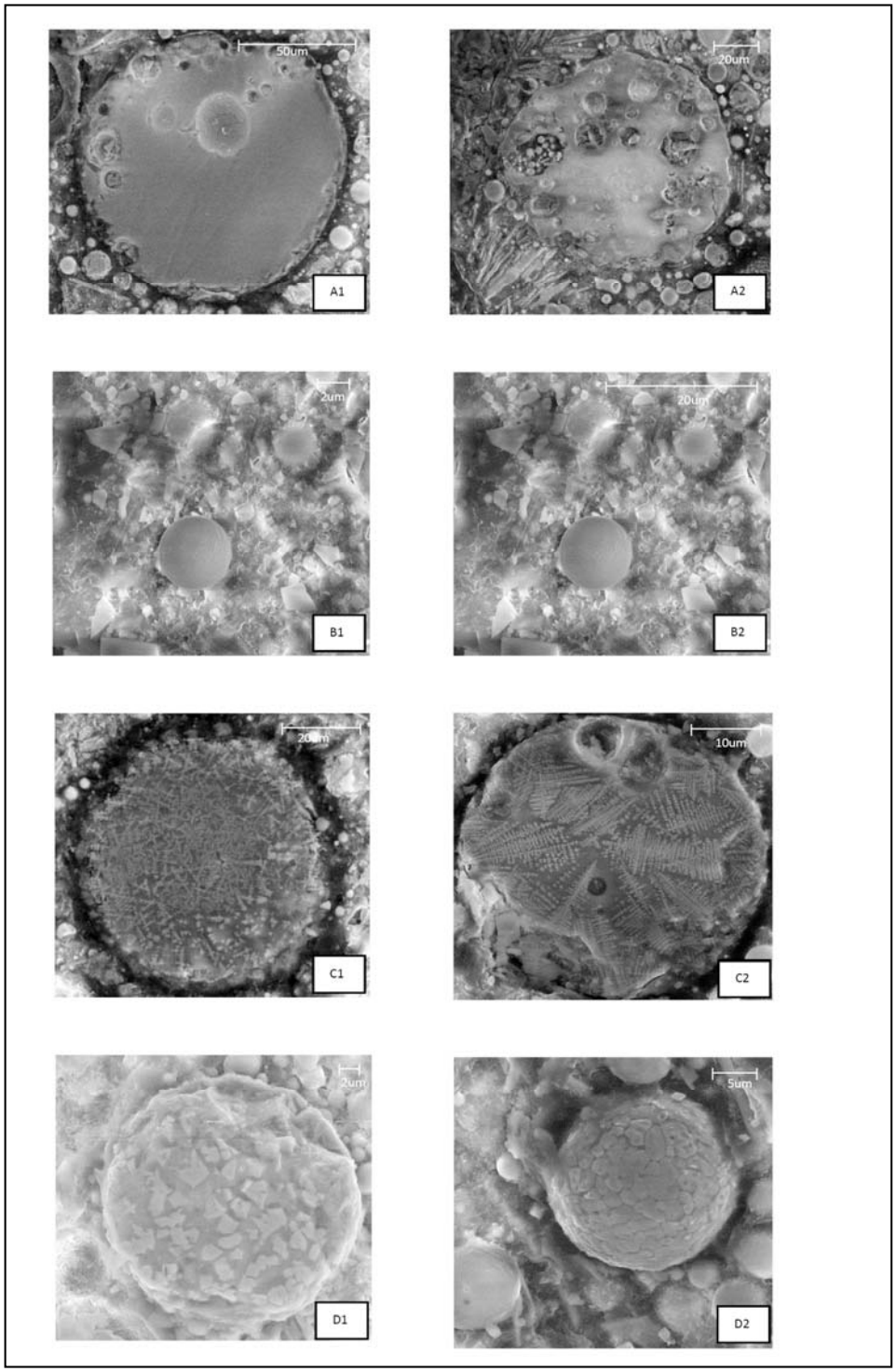

Fig. 3. Photographs of secondary electron images of different types of amorphous spheroids: (A) vesicular spheroids; (B) solid spheroids; (C) dendritic iron-coated spheroids; (D) crystalized iron-coated spheroids.

In general, amorphous spheroids, minerals (hannebachite, quartz, mullite, gypsum), and organic char were the major components identified using SEM. Despite a seemingly wide range of particle size, shape, and internal structure, observations from SEM suggested there were four different types of particles in the amorphous spheroids, including vesicular spheroids (Fig. 3A), solid spheroids (Fig. 3B), dendritic amorphous spheroids, iron-coated spheroids (Fig. 3C), and crystalized iron-coated spheroids (Fig. 3D).

Most of the spheroids had rough surfaces and exhibited various textures. Most of the amorphous phase was spheres, while agglomerated particles and irregular-shaped amorphous particles may be due to interparticle contact friction or rapid cooling. The only trace elements confirmed were barium and molybdenum; they were observed only in two of the samples and were typically associated with silica and aluminum on amorphous spheroids.

Electron microprobe analyses identified the chemical composition for the four types of amorphous particles (Table 4). Al_2O_3, SiO_2, Fe_2O_3 were the major oxides observed with other components. Vesicular spheroids (Fig. 3A) were common in all the samples analyzed; however, the distribution and size of the vesicles varied considerably, some particles being relatively solid, while others were extremely friable. The major components observed were SiO_2 (≥50 wt %) and Al_2O_3 (27–33 wt %). The second type of particle observed was a solid spheroid (Fig. 3B), which was generally free of vesicles or cavities and which was present in all samples. Their chemical compositions were similar to vesicular spheroids, with SiO_2 (⩾50 wt %) and Al_2O_3 (⩾30 wt %) being the dominant oxides. The vesicular and solid spheroids were all essentially alumino-sillicate glasses, with only minor amounts of other constituents (mostly FeO, K_2O, Na_2O, MgO, TiO_2, and CaO). The other two types of spheroids observed were iron-bearing phases, identified as dendritic iron-coated spheroid (Fig. 3C) and crystallized-coated spheroid (Fig. 3D). They were common in all the samples. Although relative amount of iron the size distribution varied from sphere to sphere, the iron oxides were the dominant components. The size of the spheroids were generally >10 μm. Two oxides identified were magnetite (Fe_3O_4) and hematite (Fe_2O_3), which is consistent with previous studies showing that iron oxides exist as a mixture or coating of alumino-silicate speheroids.[18,41] Iron in coal-combustion byproducts are derived from the decomposition and oxidation of iron-bearing minerals in coal, such as pyrite (FeS_2), siderite ($FeCO_3$), and ankerite ($CaFe(CO_3)_2$). A previous study showed that hematite was formed from the decomposition and oxidation of pyrite during high-temperature combustion; it was then dissolved by molten silicates and re-precipitated as crystalline magnetite.[42]

Table 4 Representative microprobe analyses (%) of spheroids from FSS samples

Component	Vesicular spheroid				Solid spheroid		Dendritic iron-coated spheroid					Crystalized iron-coated spheroid		
Analysis	1	2	3	4	1	2	1	2	3	4	5	1	2	3
Al_2O_3	32.90	27.73	32.99	30.84	30.02	31.65	13.80	13.94	14.90	11.72	12.03	18.98	21.74	17.75
MgO	1.26	1.47	2.36	2.27	1.60	1.25	0.24	0.12	0.17	0.41	0.42	0.74	0.57	0.83
Na2O	0.43	0.40	0.55	0.60	0.60	0.55	0.08	0.06	0.07	0.14	0.14	0.48	0.37	0.34
FeO	3.41	8.39	3.90	3.73	7.50	6.00	58.04	56.69	50.58	46.69	46.37	31.22	24.29	32.54
MnO	0.00	0.01	0.02	0.00	0.00	0.00	0.11	0.05	0.12	0.09	0.06	0.05	0.02	0.00
SiO2	58.27	54.52	54.82	56.13	52.72	53.63	24.12	24.52	29.64	26.60	26.98	38.68	34.19	42.67
P2O5	0.01	0.04	0.00	0.16	0.18	0.13	0.05	0.07	0.06	0.07	0.12	0.04	0.21	0.00
SO2	0.29	0.01	0.15	0.15	0.01	0.02	0.00	0.02	0.03	0.05	0.22	0.43	1.04	0.03
K2O	3.64	3.05	4.95	5.25	2.25	2.10	0.20	0.21	0.25	0.30	0.33	1.44	1.34	1.58
TiO2	0.74	1.00	0.59	0.41	1.50	1.25	0.24	0.21	0.21	0.79	0.75	0.82	0.64	0.87
CaO	0.77	0.58	0.53	0.51	3.87	3.50	4.80	0.24	0.35	7.78	7.91	1.24	1.39	0.96
Total	101.72	97.19	100.85	100.06	100.23	100.08	101.67	96.12	96.37	94.64	95.32	94.12	85.78	97.56

The SEM observations that silicon, iron, and aluminum were the main constituents were consistent with the elemental composition determined by X-ray fluorescence analysis.[15] Moreover, the mineralogy observed in these samples was consistent with X-ray diffraction (XRD) data.[16] The XRD data indicated that, on average, over 50% of the components in each of the samples analyzed were amorphous phase and about 20% of the sample was composed of hannebachite.

4.2 Distribution of trace elements

Several trace elements were analyzed using atomic absorption spectroscopy to understand how they were distributed in different components, which determines their solubility and mobility from FSS (Table 5, Fig. 4). The overall chemical partitioning patterns show some differences, indicating that the mobility and bioavailability of metals vary among the three elements. Previous studies suggested that the mobility of elements decrease following the order of the extraction sequence.[19, 43] The water-washable fraction represents elements adsorbed on the surface that can be easily washed off by precipitation. The exchangeable fraction includes weakly adsorbed elements by weak electrostatic bounds, and they can be released by ion-exchange processes, etc.[44] Both water-washable and exchangeable fractions represent elements that are released most readily into the environment, and thus indicate higher potential for groundwater contamination. The carbonate phase is a phase loosely bound and susceptible to change with environmental conditions, such as pH. Iron and manganese oxides are well known “sinks” for trace elements; the bonding mechanisms include co-precipitation, adsorption, surface complexation, ion exchange, and penetration of the mineral lattice, etc.[45] They are thermodynamically unstable under anoxic conditions (e.g., low Eh).[19] Organic and oxidizable-bound fractions represent trace elements that may be associated through complexation or a bioaccumulation process. However, because of the lack of organic matter in the FSS samples, most of the elements extracted during this step may have come from sulfites (hannebachite). Oxidizing conditions can lead to a release of soluble trace metals bound to this component. The last fraction, residual, represents the amorphous phase, which may hold trace elements in their internal structure. These elements are not expected to be released into groundwater over a reasonable time period under normal environment conditions.

Arsenic: The total concentrations of As in the samples analyzed varied from 21.11–55.97 mg/kg. Arsenic in FSS was strongly associated with the residual fraction, which accounted for more than 94% of the total content (Fig. 4). Minor amounts of As were held in the organic/oxidizable fraction, about 1.5% on average. Arsenic contents associated with water-washable and exchangeable fractions were very low, usually less than 1%. The amounts of As contained in carbonate phase and Fe-Mn oxide fractions were below the detection limit.

Copper: The total concentrations of Cu in the eight samples ranged from 18.02–30.90 mg/kg. Copper was mainly distributed in the carbonate fraction, which accounted for 37% on average. The second most abundant phase was the residual fraction, which

accounted for an average of 30%. The Fe-Mn oxide fraction accounted for approximately 19%, while the organic/ oxidizable fraction was of minor importance, having only around 9% of the total Cu in FSS. The water-washable and exchangeable fractions had very low Cu concentrations, about 2.6% and 2.3%, respectively.

Zinc: The total concentrations of Zn varied from 97.95–135.75 mg/kg. Figure 4 shows that the highest proportions of Zn were associated with the residual fraction (average 56.3%). Carbonate phase, Fe-Mn oxide, and organic/oxidizable fractions were next, accounting for 22.5%, 12.8%, and 7.4%, respectively. The percentage of the water-washable and exchangeable fractions is very low in FSS, less than 1% on average.

The sequential extractions elucidate the distribution and leachability of several trace elements in FSS. The leaching behavior of As, Cu, and Zn differed because they each were bonded to different fractions. For all three elements, only minor amounts came from the water-washable or exchangeable fractions, which are considered easily available under neutral conditions and presents the greatest threat of contamination to groundwater. We detected significant amounts of copper and zinc in the carbonate and Fe-Mn oxide fractions; Cu and Zn become unstable under acidic or reducing conditions, which is usually the case in AML sites. The elements associated with the aluminosilicate matrix (i.e., the residual fraction) were difficult to leach under natural conditions, and thus present the lowest threat to groundwater. Based on our findings, the relative solubility and mobility of the three elements decrease in the following order: Cu>Zn>As.

Table 5 Distribution of As, Cu, and Zn in FSS according to six sequential extraction procedures (ppm)

Element	Extraction steps	Samples							
		M7-02-t	M7-02-b	M7-03-m	M7-03-b	M8-02-t	M8-02-b	M8-03-m	M8-03-b
As	Ex-1	0.019556	0.054584	0.066876	0.072525	0.065509	0.276632	0.068425	0.033122
	Ex-2	0.172013	0.246692	0.160268	0.250112	0.063215	b.d.	0.229430	b.d.
	Ex-3	b.d.	b.d.	b.d.	b.d.	b.d.	b.d.	b.d.	b.d.
	Ex-4	b.d.	b.d.	b.d.	b.d.	b.d.	b.d.	b.d.	b.d.
	Ex-5	0.909204	0.95231	0.618853	0.621789	b.d.	0.164152	0.347288	0.088301
	Ex-6	20.00865	36.17631	36.28601	26.67678	53.67187	55.53207	39.24815	30.50843
Cu	Ex-1	0.523821	0.734082	0.75141	0.471392	0.698952	0.592659	0.716032	0.643318
	Ex-2	0.568720	0.519351	0.569175	0.428992	0.549176	0.657403	0.538895	0.556384
	Ex-3	9.740584	7.453184	10.60962	8.293011	11.02097	9.57468	7.497131	6.867859
	Ex-4	3.711649	4.234707	3.694643	4.130294	6.030954	5.060013	5.927848	4.987581
	Ex-5	1.920678	1.722846	2.446453	2.095077	2.396405	1.942328	3.293249	1.440636
	Ex-6	1.551257	14.8919	8.233703	3.210014	8.553915	13.07789	6.920135	8.031433
Zn	Ex-1	0.192068	0.332085	0.454341	b.d.	b.d	b.d.	b.d.	0.278192
	Ex-2	1.456722	1.068664	1.298118	1.127351	1.078382	0.886498	1.017913	1.092896
	Ex-3	31.77850	24.86891	31.74147	20.48935	28.75686	28.8859	25.54763	20.40487
	Ex-4	13.76902	13.54307	14.15947	12.25121	19.87019	14.72185	17.12489	15.45951
	Ex-5	11.37441	7.490637	9.511209	9.128548	8.212681	6.698541	8.507560	7.029309
	Ex-6	39.37755	86.57503	73.63949	55.41266	72.59158	84.55381	65.10381	64.13332

Note: Ex-1: water-washable; Ex-2: exchangeable; Ex-3: carbonate bound; Ex-4: Fe-Mn oxide bound; Ex-5: organic and oxidizable bound; Ex-6: residual.

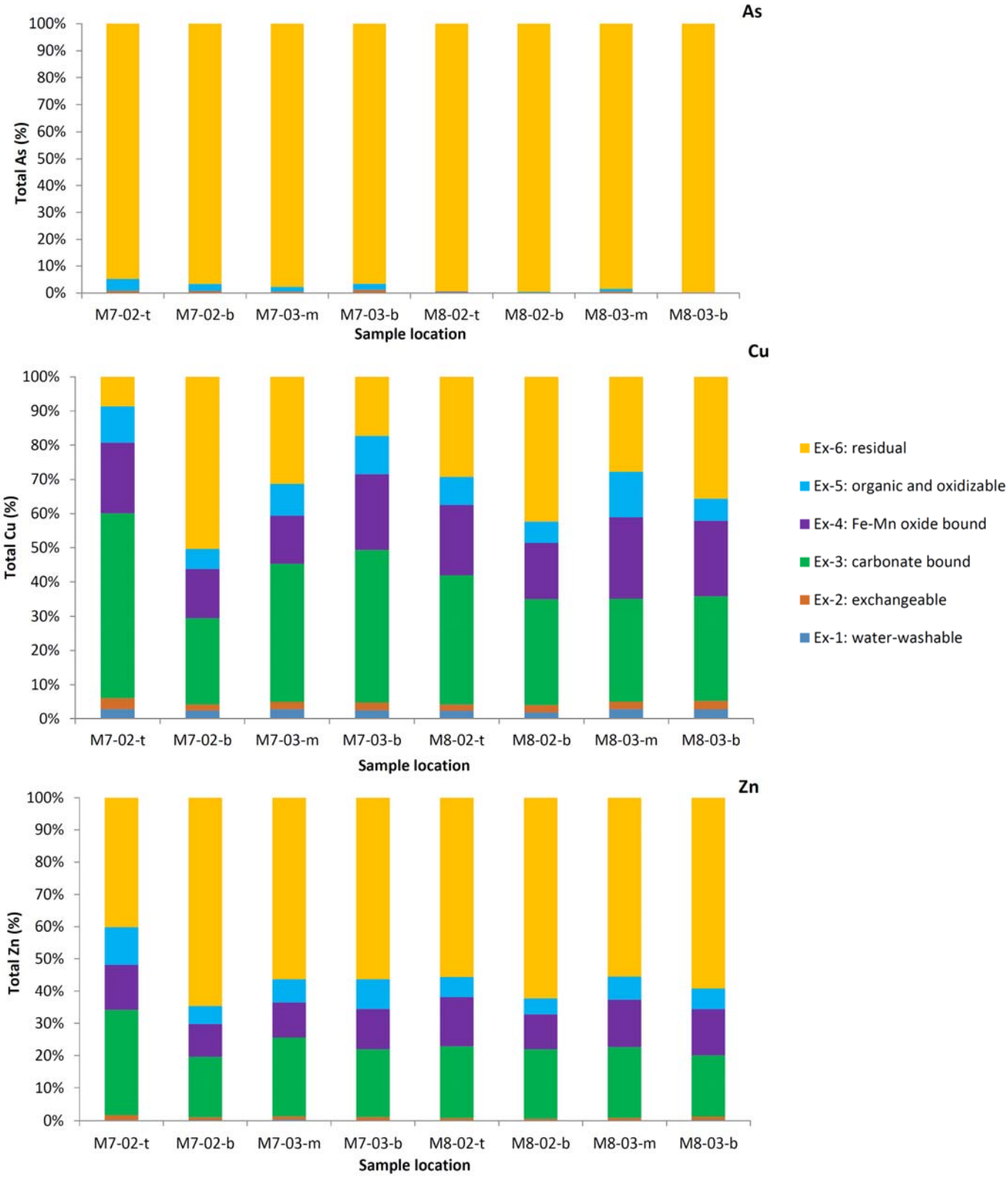

Fig. 4. Relative distributions of As, Cu, and Zn in different fractions.

4.3 Preliminary simulations

4.3.1 Aqueous chemistry

The simulated lateral profiles of pH show step-wise pH fronts caused by buffering reactions (Fig. 5a,b).[46] These zones propagate downstream as time progresses. For the ambient groundwater simulation, pH increases from the initial value of 6.1 to approximately 7.0 within one year because of the effects of mineral alteration; yet no pH front is observed at this interval. The pH front propagates to nearly 2 m within 20 years and to slightly more than 6 m within 100 years. By contrast, FSS responds quicker to acid water influx, as pH decreases to AMD levels over 4 m of the flow domain within just one year, and the initial pore water completely changes by AMD within ten years. An acidified zone extends with the progressive pH front. However, the final pH value is higher than the anoxic mine inflow (pH 1.8), indicating that a moderate amount of alkalinity was generated by the FSS system.

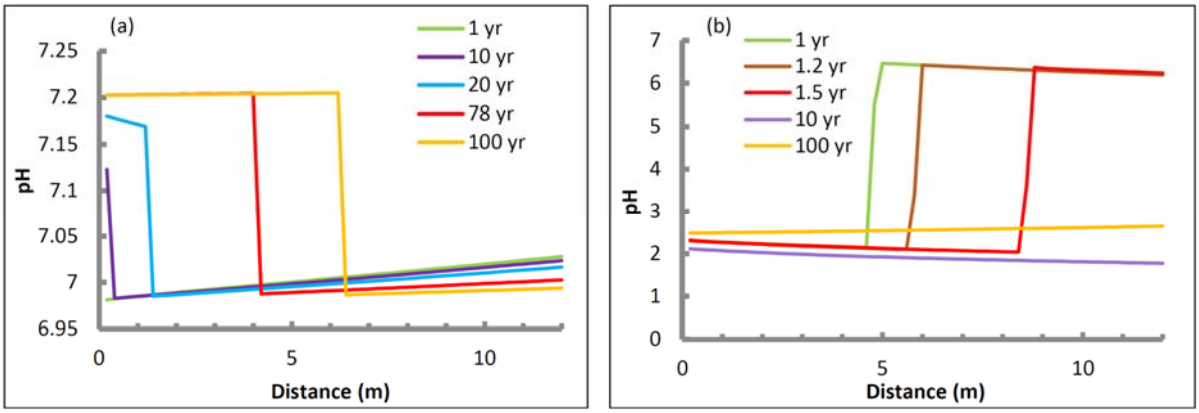

Fig. 5 Line graphs comparing pH evolutions for ambient groundwater (a) and acid mine drainage water (b) at different times.

In our preliminary simulations, alkalinity was generated from the dissolution of calcite, corresponding closely with pH, which also shows step-wise behavior (Fig. 6 a,b). In the case of ambient groundwater, alkalinity increases with time while pH increases. For anoxic mine water, more alkalinity was generated by the dissolution of calcite, but the alkalinity was quickly depleted by the acidic water. Note that it drops to zero after ten years when pH reaches about 2.0.

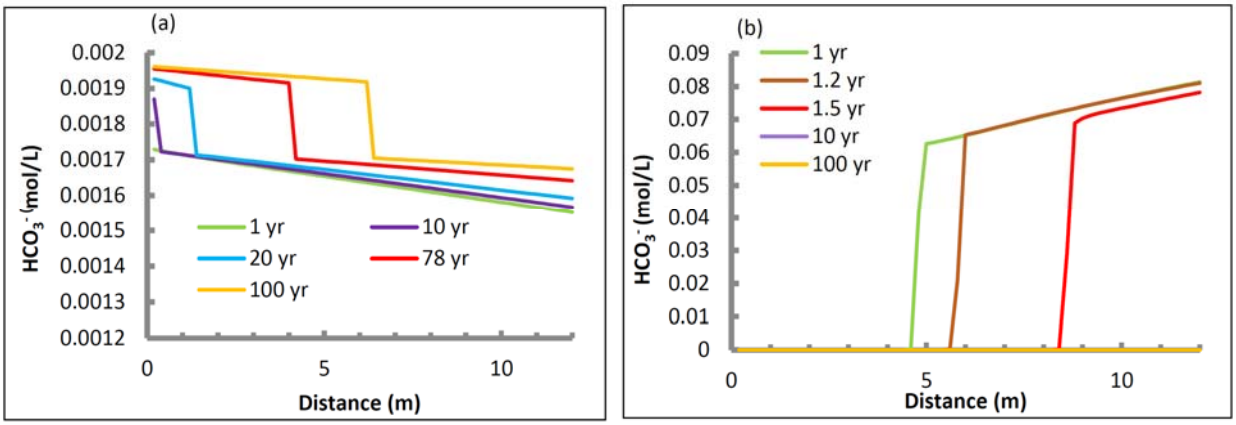

Fig.6. Line graphs of alkalinity variations for ambient groundwater (a) and AMD water (b) at different times.

Aqueous sulfate is the dominant dissolved species in the FSS system, which, in preliminary simulations, also shows a step-wise evolution over the lateral distance (Fig. 7a,b). In the ambient groundwater simulation, aqueous sulfate concentration decreases with time owing to increased pH; by contrast, sulfate concentration is much higher in anoxic mine water and increases over time. The migration fronts exhibited by both bicarbonate and sulfate reflect the pH distributions in the preliminary work.

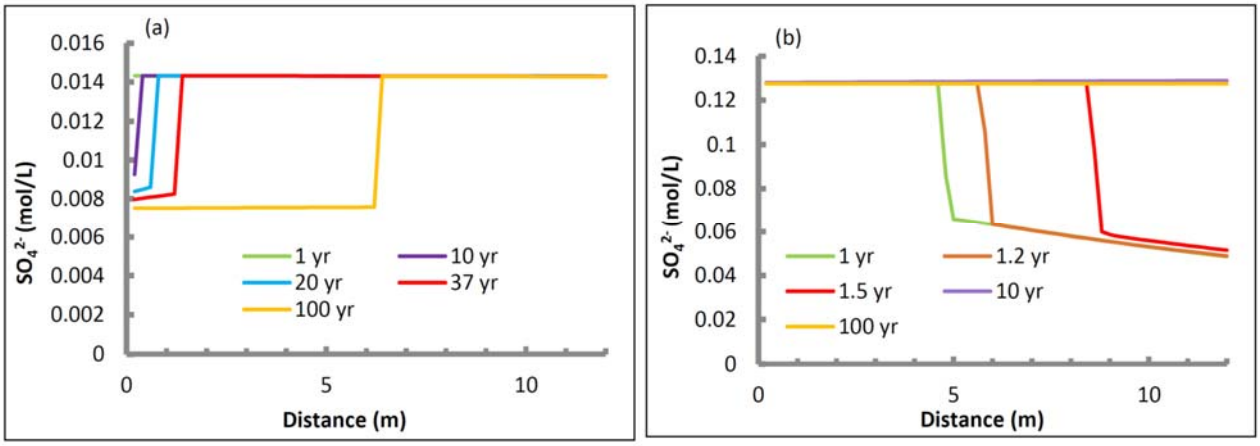

Fig.7. Line graphs of aqueous concentrations of sulfate for ambient groundwater (a) and AMD water (b) at different times.

4.3.2 Solid phases

Calcite behavior is subject to the pH conditions of the two inflows (Fig. 8a,b). In the case of ambient groundwater, calcite doesn't change much during the first ten years, but it starts to precipitate in the first few meters during the simulated domain because of increased pH after ten years. This is expected because carbonates are stable at a higher pH (around 6). On the other hand, in the case of anoxic mine water, progressive calcite dissolution is observed within the acidified zone through the first few years of simulation. This is caused by a decrease in pH and corresponding increase of sulfate. By year 2, all available calcite in the permeable thin layer is dissolved owing to its fast dissolution rate, and the calcium ions have combined with sulfate to facilitate gypsum formation.

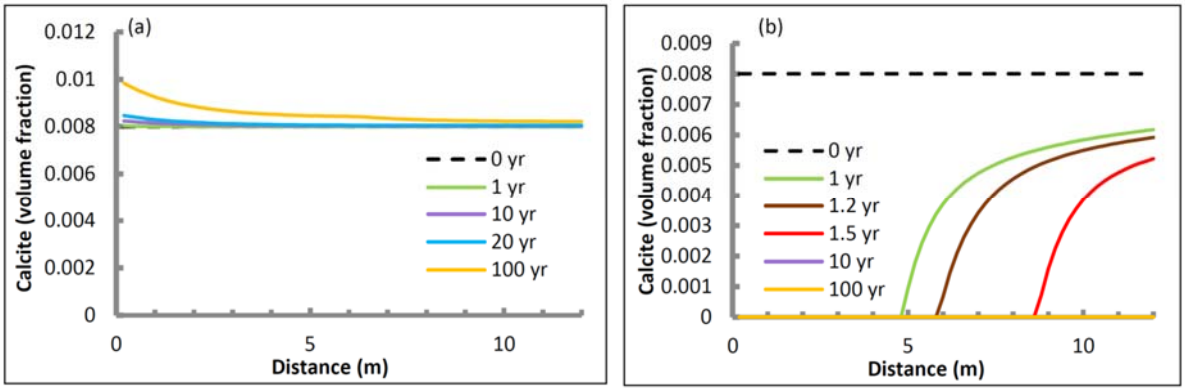

Fig. 8. Line graphs of the variation in calcite abundance for ambient groundwater (a) and AMD water (b) over time.

Hannebachite reacts faster with ambient groundwater than with anoxic water, which is expected because it converts to gypsum with the presence of oxygen (Fig. 9a,b). By contrast, hannebachite reacts slower and has a higher remaining volume percentage in the anoxic water simulation (Fig. 10). Note that hannebachite is completely depleted after 75 years in the ambient groundwater simulation and within 100 years in the anoxic mine water simulation. Another factor to consider is that hannebachite has a very small change of volume percentage across the 12-m solution domain. This result requires further investigation about how changes in the kinetic rate affect hannebachite dissolution, because kinetic rate data is not currently available in the published literature.

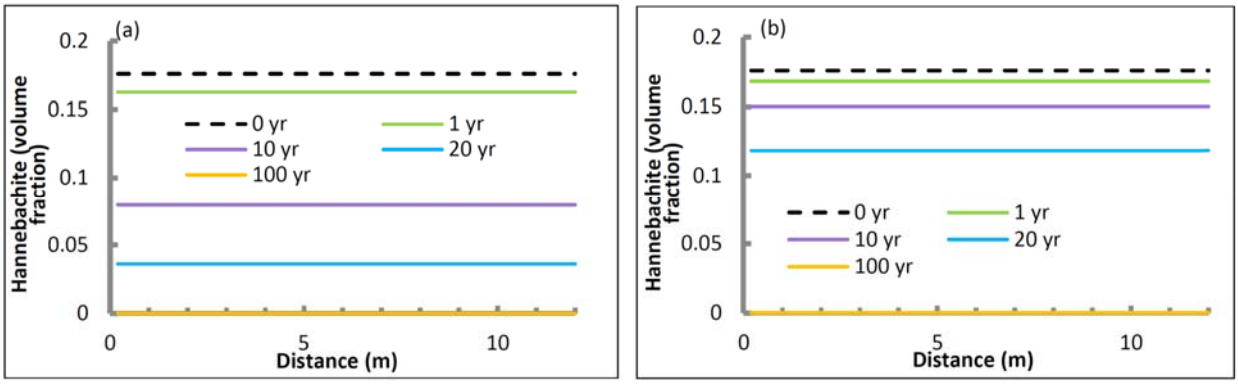

Fig. 9. Line graph of the variation of hannebachite abundance for ambient groundwater (a) and AMD water (b) over time.

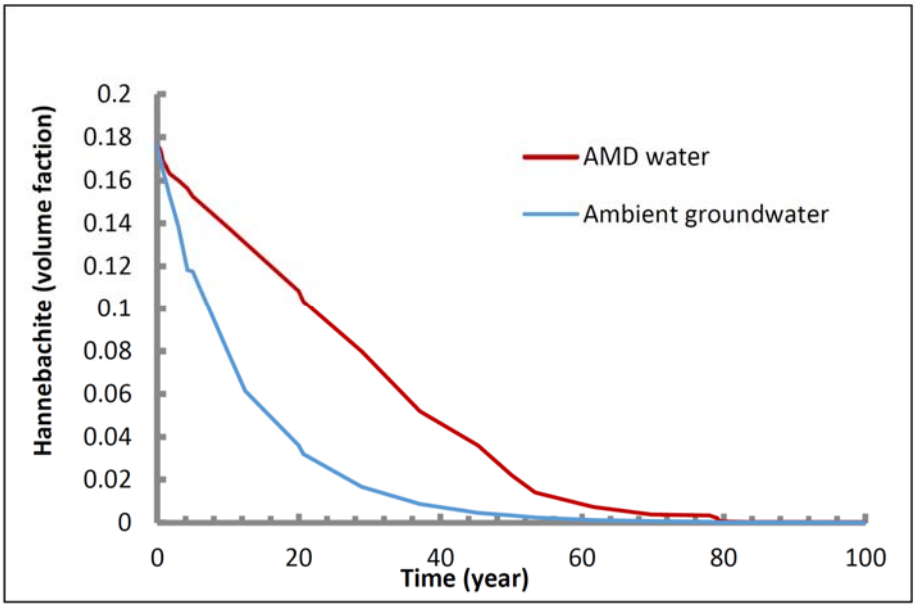

Fig. 10. Line graph showing hannebachite volume fractions over time in the presence of ambient groundwater and anoxic mine water. The unsmooth curves probably indicate numerical noise, which may require further investigation.

5 Conclusions

This study examined the morphology and chemistry of the particles in fixated scrubber sludge that was used as a capping material for the Midwestern abandoned mine land site reclamation project, completed in 1996. Morphological analyses show that the FSS contains four different types of amorphous particles (Fig. 3), including vesicular spheroids, solid spheroids, dendritic iron-coated spheroids, and crystalized iron-coated spheroids. Chemical analyses reveal that the amorphous phase consists mostly of alumino-silicate spheroids with iron coating on some of the spheres. To enhance the modeling of long-term effects of using FSS as a capping material at an abandoned mine lands site, more detailed chemical analyses of amorphous phases were conducted using an electron microprobe (Table 4). These data, coupled with sequential extraction procedures, provided more information about trace element mineral phase distribution and mobility than data from bulk concentration analyses. To date, the distribution and relative mobility of As, Cu, and Zn have been determined, with Cu showing the most mobility owing to a higher concentration in carbonate mineral phases, and As having the least potential for mobility, because it is concentrated in the much less reactive alumino-silicate residues. Further analyses of trace elements (B, Ba, Pb, Cr, and Ni) are in progress. Because of the existence of many different sequential extraction procedures, comparing these results with other studies is problematic, given that there are limited number of studies conducted on sequential extraction of coal-combustion byproducts, especially FSS.[19, 46] This analytical work is essential for preparing and providing the prerequisite information necessary for subsequent numerical simulations.

The numerical simulations provide basic insights regarding the chemical reactions of FSS materials when they interact directly with ambient groundwater and anoxic mine water. Preliminary modeling demonstrates that FSS can buffer acid mine drainage by generating moderate alkalinity. Primary minerals are dissolved, especially when the FSS is in contact with acidic mine water. Hannebachite becomes oxidized to gypsum at a faster rate under ambient groundwater flow because of higher oxygen content dissolved in the flow. Secondary clay minerals (e.g., kaolinite), hydroxides (e.g., gibbsite), and amorphous silica precipitation were observed in the preliminary modeling work. However, the current results are constrained in that no trace elements were included. Therefore, our future work will focus on developing a reactive transport model coupled with surface complexation of trace elements; this work will include modeling the dissolution of trace elements in the FSS, recording the subsequent reactions (re-precipitation with other minerals or surface adsorption onto hydroxides), and the possible sequestering of trace elements already existing in AMD water. Moreover, we will conduct comprehensive sensitivity analyses to encompass all possible conditions and scenarios that are encountered at a typical AML reclamation site. The ultimate goal of this study is to obtain detailed information on the geochemical properties of FSS, and thus provide quantitative predictions and valuable insights into the long-term feasibility and potential risk associated with using FSS as mine reclamation materials.

References:

[1] American Coal Ash Association (ACAA), 2011. Revised 2009 CCP Production & Use Survey Report. http:www.acaausa.org/associations/8003/files/2009_Production_and_Use_Survey_Revised_100511.pdf. Accessed Feburary 8th, 2014.

[2] Vassilev, S. Trace elements in solid waste products from coal burning at some Bulgarian thermoelectric power stations. Fuel, 1994, 73, pp. 367–374.

[3] Vassilev, S. and Vassileva, C. Mineralogy of combustion wastes from coal-fired power stations. Fuel Processing Technology, 1996, 47, pp. 261–280.

[4] Vassilev, S. and Vassileva, C. Geochemistry of coals, coal ashes and combustion wastes from coal-fired power stations. Fuel Processing Technology, 1997, 51, pp.19–45.

[5] Querol, X., Fernández-Turiel, J., and López-Soler, A. Trace elements in coal and their behaviour during combustion in a large power station. Fuel, 1995, 74, pp. 331–343.

[6] Querol, X., Juan, R., Lopez-Soler, A., Fernandez-Turiel, J.L., and Ruiz, C.R. Mobility of trace elements from coal and combustion wastes. Fuel, 1996, 75, pp. 821–838.

[7] Martinez-Tarazona, M.R. and Spears, D.A. The fate of trace elements and bulk minerals in pulverized coal combustion in a power station. Fuel Processing Technology, 1996, 47, pp. 79–92.

[8] Karayigit, A.I., Onacak, T., Gayer, R.A., and Goldsmith, S. Mineralogy and geochemistry of feed coals and their combustion residues from the Cayirhan power plant, Ankara, Turkey. Applied Geochemistry, 2001, 16, pp. 911–919.

[9] Vassilev, S., Menendez, R., Alvarez, D., Diaz-Somoano, M., and Martinez-Tarazona, M.R. Phase-mineral and chemical composition of coal fly ashes as a basis for their multicomponent utilization: 1. Characterization of feed coals and fly ashes. Fuel, 2003, 82, pp. 1793–1811.

[10] Kutchko B.G. and Kim, A.G. Fly ash characterization by SEM-EDS. Fuel, 1996, 85, pp. 17–18.

[11] Vassilev, S.V. and Vassileva, C.G. Methods for characterization of composition of fly ashes from coal-fired power stations: a critical overview. Energy and Fuels, 2005, 19, pp. 1084–1098.

[12] Sajwan K.S., Punshon, T., Seaman, J.C., and Alva, A.K. Coal Combustion Byproducts and Environmental Issues: New York, Springer Science-Business Media, 2006, pp. 3–20.

[13] Smith, C.L. Physical aspects of FGD by-products. International Journal of Environmental Issues in Minerals and Energy Industry, 1992, 1, pp. 37–46.

[14] Butalia, T. and Wolfe, W.E. Evaluation of permeability characteristics of FGD materials. Fuel, 1999, 2, pp. 149–152.

[15] Martin, L.C., Branam, T.D., Naylor, S., and Olyphant, G.A. Characterization of coal combustion byproducts fifteen years after emplacement in an abandoned mine land site. Proceedings of American Society of Mining and Reclamation, Tupelo, MS, Sustainable Reclamation, Lexington, KY, June 8-15, 2012.

[16] Martin, L.C., Branam, T.D., Naylor, S., and Olyphant, G.A. Weathering and leaching characteristics of a fixated scrubber sludge cap at an abandoned mine site in Pike County, Indiana. Proceeding of World of Coal Ash Conference, Lexington, KY, April 22–25, 2013.

[17] Bryenton, D. L. and J. H. Gasper. Design and construction guidelines for coal combustion by-product utilization in abandoned mine land settings - a case study. Proceedings of Coal Combustion By-Products Associated with Coal Mining - Interactive Forum, Carbondale, IL, October 29–31, 1996.

[18] Gomes, S., Francois, M., Abdelmoula, M., Refait, P., Pellissier, C., and Evrard, O. Characterization of magnetite in silico-aluminous fly ash by SEM, TEM, XRD, magnetic susceptibility, and Mossbauer spectroscopy. Cement and Concrete Research, 1999, 29, pp. 1705–1711.

[19] Tessier, A., Campbell, P.G.C., and Bisson, M. Sequential extraction procedure for the speciation of particulate trace metals. Analytical Chemistry, 1979, 51, pp. 844–851.

[20] Smeda, A. and Zyrnicki, W. Application of sequential extraction and the ICP-ADS method for the study of the portioning of metals in fly ashes. Microchemical Journal, 2002, 72, pp. 9–16.

[21] Pruess, K. The TOUGH codes-a family of simulation tools for multiphase flow and transport processes in permeable media. Vadose Zone Journal, 2004, 3, pp. 738–746.

[22] Wolery, T. J. EQ3NR: A computer program for geochemical aqueous speciation-solubility calculations. In: User's Guide and Documentation. Lawrence Livermore National Lab, CA, 1983.

[23] Xu, T., Sonnenthal, E., Spycher, N., and Pruess, K. TOUGHREACT user’s guide: A simulation program for nonisothermal multiphase reactive geochemical transport in variably saturated geologic media. Lawrence Berkeley National Laboratory, 2004, Paper LBNL-55460.

[24] Xu, T. F., Gerard, F., Pruess, K., and Brimhall, G. Modeling nonisothermal multiphase multispecies reactive chemical transport in geologic media. Lawrence Berkeley Laboratory, 1997, Report LBL-40504, p. 79.

[25] Xu, T. F., Pruess, K., and Brimhall, G. An improved equilibrium-kinetics speciation algorithm for redox reactions in variably saturated subsurface flow systems. Computers & Geosciences, 1999, 25, pp. 655–666.

[26] Steefel, C.I. and Lasaga, A.C. A coupled model for transport of multiple chemical species and kinetic precipitation/dissolution reactions with applications to reactive flow in single phase hydrothermal system. American Journal of Science, 1994, 294, pp. 529–592.

[27] Xiao, Y.T., Xu, T.F., and Pruess, K. The effects of gas-fluid-rock interactions on CO2 injections and storage: Insights from reactive transport modeling. Energy Procedia, 2009, 1, pp. 1783–1790.

[28] Marsily, G.de. Quantitative Hydrogeology: New York, Academic Press, 1986, p. 464.

[29] Palandri, J. L. and. Kharaka, Y. K. A compilation of rate parameters of water-mineral interaction kinetics for application to geochemical modeling. U.S. Geological Survey Open-File Report 2004-1068, 2004.

[30] Perkins, R. B. and Palmer, C.D. Solubility of ettringite ($Ca_6[Al(OH)_6]_2(SO4)_3 \cdot 26H_2O$) at 5–75°C. Geochimica et Cosmochimica Acta, 1999, 63, pp. 1969–1980.

[31] Myneni, S C.B., Traina, S.J., and Logan, T.J. Ettringite solubility and geochemistry of the $Ca(OH)_2$–$Al_2(SO_4)_3$–H_2O system at 1 atm pressure and 298 K. Chemical Geology, 1998, 148, pp. 1–19.

[32] Cohen, A. and Zangen, M. Studies on alkaline earth sulfites – III [1]. Transient solubilities and phase changes of calcium sulfite in seawater. Desalination, 1982, 41, pp. 215–232.

[33] Waldbaum, D. R. Thermodynamic properties of mullite, andalusite, kyanite and sillimanite. The American Mineralogist, 1965, 50, pp. 186–195.

[34] Oelkers, E. H. and Gislason, S.R. The mechanism, rates and consequences of basaltic glass dissolution: I. An experimental study of the dissolution rates of basaltic glass as a function of aqueous Al, Si and oxalic acid concentration at 25°C and pH 3 and 11. Geochimica et Cosmochimica Acta, 2001, 65, pp. 3671–3681.

[35] Sonnenthal, E., Ito, A., Spycher, N., Yui, M., Apps, J., Sugita, Y., Conrad, M., and Kawakami, S. Approaches to modeling coupled thermal, hydrological, and chemical processes in the Drift Scale Heater Test at Yucca Mountain. International Journal of Rock Mechanics and Mining Sciences, 2005, 42, pp. 698–719.

[36] Baur, I., Keller, P., Mavrocordatos, D., Wehrli, B., and Johnson, C.A. Dissolution-precipitation behaviour of ettringite, monosulfate, and calcium silicate hydrate. Cement and Concrete Research, 2004, 34, pp. 341–348.

[37] Taerakul, P., Sun, P., Golightly, D.W., Butalia, T., Walker, H.W., and Weavers, L.K. Characterization of Hg, As, and Se in Lime Spray Dryer Ash. Internaional Ash Utilization Symposium, Center for Applied Energy Research, University of Kentucky, 2003, Paper #73.

[38] She, J. H. and Ohji, T. Fabrication and characterization of highly porous mullite ceramics. Materials Chemistry and Physics, 2003, 80, pp. 610–614.

[39] Bullard, J. W., Enjolras, E., George, W.L., Satterfield, S.G., and Terrill, J.E. A parallel reaction-transport model applied to cement hydration and microstructure development. Modeling and Simulation in Materials Science and Engineering, 2010, 18, pp. 1–16.

[40] Hao, Y. L. and Dick, W.A. Potential inhibition of acid formation in pyritic environments using calcium sulfite byproduct. Environmental Science & Technology, 2000, 34, pp. 2288–2292.

[41] Zhao, Y.C., Zhang, J.Y., Sun, J.M., Bai, X.F., and Zheng, C.G. 2006. Mineralogy, chemical composition, and microstructure of ferrospheres in fly ashes from coal combustion.Energy and Fuels, 20, pp. 1490–1497.

[42] Xue, Q.F. and Lu, S.G. Microstructure of ferrospheres in fly ashes: SEM, EDX and ESEM analysis. Journal of Zhejiang University Science A, 2008, 9, pp. 1595–1600.

[43] Rao, C.R.M., Sahuquillo, A., and Lopez Sanches, J.F. A Review of the Different Methods Applied in Environmental Geochemistry for Single and Sequential Extraction of Trace Elements in Soils and Related Materials. Water Air & Soil Pollution, 2008, 189, pp. 291–333.

[44] Krishnamurti, G.S.R., Huang, P.M., Van Rees, K.C.J., Kozak, L.M., and Rostad, H.P.W. Speciation of particulate-bound cadmium of soils and its bioavailability. Analyst, 1995, 120, pp. 659–665.

[45] Hall, G. E. M., Gauthier, G., Pelchat, J. C., Pelchat, P., and Vaive, J. E. Application of a sequential extraction scheme to ten geological certified reference materials for the determination of 20 elements. Canadian Journal of Analytical Atomic Spectrometry, 1996, 11, pp. 787–796.

[46] Helfferich, F. G. The theory of precipitation/dissolution waves. AIChE Journal, 1989, 35, pp. 75–87.

[47] Bodog, I., Polyak, K., Csikos-Hartyanyi, Z., and Hlavay, J. Sequential extraction procedure for the speciation of elements in fly ash samples. Microchemical Journal, 2001, 54, pp. 1015–1020.